Rapid Communications

# Vorticity fluxes and secondary flow: Relevance for turbulence modeling

A. Vidal,[1,*] H. M. Nagib,[1] and R. Vinuesa[2]
[1]*MMAE Department, Illinois Institute of Technology, Chicago, Illinois 60616, USA*
[2]*Linné FLOW Centre, KTH Mechanics and Swedish e-Science Research Centre (SeRC), Stockholm, Sweden*

(Received 25 March 2018; published 12 July 2018)

Vorticity fluxes are analyzed in fully developed turbulent flow through rectangular ducts with a width-to-height ratio of 3, and both straight and semicylindrical side walls, at a centerplane friction Reynolds number $\mathrm{Re}_{\tau,c} \simeq 180$. The transport of secondary Reynolds stresses by the secondary flow of Prandtl's second kind is analyzed from a vorticity-flux perspective. This analysis reveals that the in-plane transport of viscous stresses locally counteracts the inhomogeneous distribution of the turbulent shear-stress gradient in the spanwise direction. A relationship is established between the mean and fluctuating transport terms that can be useful to improve turbulence models and their ability to accurately predict the secondary flow. Finally, quadrant analysis is used to evaluate the contribution from the different types of bursting events to the fluctuating transport terms.

DOI: 10.1103/PhysRevFluids.3.072602

The connection between the vorticity fluxes and the primary Reynolds shear stress was first considered by Taylor [1], and it has been used in a number of flow cases, including turbulent wakes [2] and plane channels [3]. The vorticity-transport perspective can be useful to study the transfer of viscous stress to Reynolds stress in the near-wall region. This analysis framework was used by Eyink [4] to study the role of the flux of spanwise vorticity in pipe and channel flows. Furthermore, the vorticity fluxes in turbulent channel flow were recently analyzed by Brown *et al.* [5] and in plane Couette flow by Brown [6], where the important role of the streamwise vorticity and the near-wall quasistreamwise vortices were discussed.

In the present study, this analysis is extended to fully developed turbulent flow through rectangular ducts with straight and semicylindrical sidewalls and aspect ratio $AR = 3$, defined as the total width of the duct divided by its total height. The main difference between the rectangular duct and the plane channel flow is the presence of vertical sidewalls, which introduce three-dimensional effects such as boundary-layer growth in the spanwise direction and secondary motions of Prandtl's second kind [7]. The term *secondary motions* refers to the nonzero mean velocity components in the vertical $V$ and spanwise $W$ directions, which are normal to the mean streamwise velocity $U$. The relationship between the vorticity-flux terms $\overline{v'\omega'_z}$ and $\overline{w'\omega'_y}$, and the primary Reynolds shear stresses $\overline{u'v'}$ and $\overline{u'w'}$ is shown in Eq. (1) for fully developed turbulent flow through a rectangular duct. In this equation, $y$ and $z$ are the vertical and spanwise directions; $u'$, $v'$, and $w'$ are the streamwise, vertical, and spanwise fluctuating velocities, and $\omega'_y$ and $\omega'_z$ are the vertical and spanwise fluctuating vorticities, respectively. Note that in plane channel and Couette flows the second term on the left-hand side of the equation is zero since the flow is homogeneous in the spanwise direction. Interestingly, Eq. (1) is also valid for the mean velocity components in fully developed turbulent flow with secondary motions, as shown in Eq. (2). The continuity equation and $\partial(\cdot)/\partial x = 0$ (where $x$ is the streamwise direction) due to the fact that the flow is fully developed are used to cancel the terms in Eq. (2). Since this relation is separately valid for the fluctuating and averaged quantities, it must also be valid for

*avidalto@hawk.iit.edu

 

TABLE I. Summary of the cases under study, where $r/h$ is the rounding radius of the sidewalls, $\mathrm{Re}_b$ is the Reynolds number based on the bulk velocity and the half-height of the duct, $\mathrm{Re}_{\tau,c}$ is the friction Reynolds number based on the friction velocity at $z/h = 0$, and $t_a U_b/h$ is the averaging time expressed in convective time units.

| Case | $AR$ | $r/h$ | $\mathrm{Re}_b$ | $\mathrm{Re}_{\tau,c}$ | Number of fields | $t_a U_b/h$ |
|---|---|---|---|---|---|---|
| AR3r0 | 3 | 0 | 2581 | 179 | 334 | 5664 |
| AR3r1 | 3 | 1 | 2800 | 191 | 700 | 1400 |

the corresponding time average of the instantaneous products [see Eq. (3)]. This was reported by Klewicki [8] for turbulent channel flows, where the second term on the left-hand side is zero. Note that lowercase letters without primes are used to refer to the instantaneous components.

$$\frac{\partial \overline{u'v'}}{\partial y} + \frac{\partial \overline{u'w'}}{\partial z} = \overline{w'\omega_y'} - \overline{v'\omega_z'}. \tag{1}$$

$$\frac{\partial (UV)}{\partial y} + \frac{\partial (UW)}{\partial z} = U\cancelto{0}{\left(\frac{\partial V}{\partial y} + \frac{\partial W}{\partial z}\right)} + V\frac{\partial U}{\partial y} + W\frac{\partial U}{\partial z} = W\Omega_y - V\Omega_z,$$

$$\Omega_y = \frac{\partial U}{\partial z} - \cancelto{0}{\frac{\partial W}{\partial x}}, \tag{2}$$

$$\Omega_z = \cancelto{0}{\frac{\partial V}{\partial x}} - \frac{\partial U}{\partial y}.$$

$$\frac{\partial \overline{uv}}{\partial y} + \frac{\partial \overline{uw}}{\partial z} = \overline{w\omega_y} - \overline{v\omega_z}. \tag{3}$$

The main characteristics of the cases under study are shown in Table I. The results were obtained from direct numerical simulations using the spectral-element code Nek5000 developed by Fischer *et al.* [9] at the Argonne National Laboratory. The setup of the simulations is described by Vinuesa *et al.* [10] and Vidal *et al.* [11] for the ducts with straight and semicylindrical sidewalls, respectively. The results presented in this work were calculated from the instantaneous velocity fields generated in these two studies, thus, there is a discrepancy between the number of samples and averaging periods. However, the turbulence statistics are sufficiently converged to compare both cases.

Analyzing the behavior of the fluctuating, mean and instantaneous vorticity fluxes in rectangular ducts can help us better understand the relationship between the secondary flow and the turbulent shear stresses. The fluctuating vorticity-flux terms on the vertical centerplane ($z/h = 0$) are shown in Fig. 1 (left) for the two cases under consideration. On this plane $\overline{u'w'} = 0$ due to symmetry, and the results are in good agreement with the channel case at $\mathrm{Re}_\tau = 1000$ shown in Fig. 1 from Brown *et al.* [5]. Note that at the walls (located at $y/h = \pm 1$) these terms must be zero due to the no-slip condition and, from Eq. (1), $\overline{u'v'} = \partial \overline{u'v'}/\partial y = 0$. In a region close to the wall, i.e., approximately for $y^+ < 10$, the vorticity transport terms have opposite signs ($\overline{w'\omega_y'} < 0$, $\overline{v'\omega_z'} > 0$) such that both terms contribute to the negative Reynolds shear-stress gradient $\partial \overline{u'v'}/\partial y < 0$. After $y^+ \simeq 10$ the vertical-transport term becomes negative, $\overline{v'\omega_z'} < 0$, opposing the stronger spanwise-transport term $\overline{w'\omega_y'}$. At $y^+ \simeq 30$ both terms have the same magnitude, and approximately at this wall-normal location the $\overline{u'v'}$ must also reach its maximum value [see Eq. (1)]. In the channel case at $\mathrm{Re}_\tau = 1000$ [5], the critical value of $y^+$ where $\overline{w'\omega_y'} = \overline{v'\omega_z'}$ is located farther away from the wall, at $y^+ \simeq 50$, as a direct consequence of its higher $\mathrm{Re}_{\tau,c}$ value [12]. Note that the features of the profiles that are being

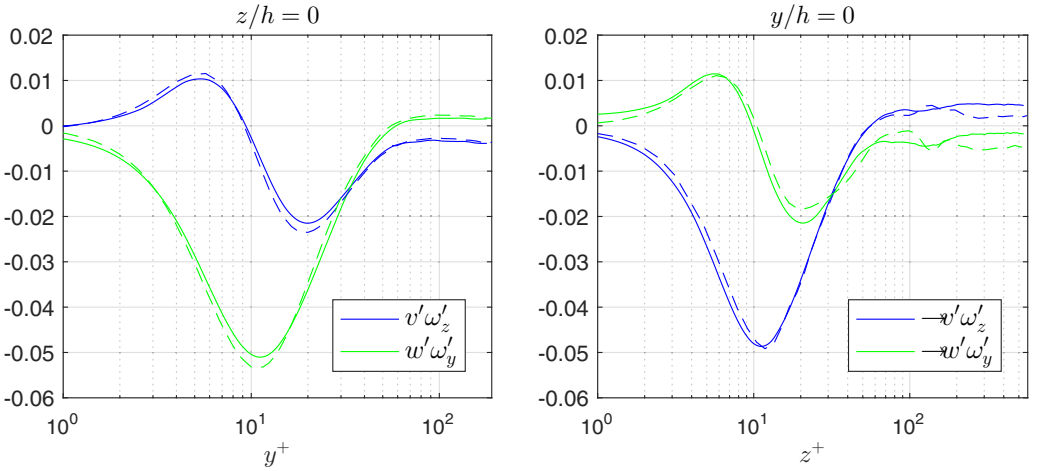


FIG. 1. Vorticity-flux terms $\overline{v'\omega_z'}^+$ and $\overline{w'\omega_y'}^+$ on the (left) vertical and (right) horizontal symmetry planes scaled with the kinematic viscosity $\nu$ and the local friction velocity $u_\tau$. The results from the AR3r0 and AR3r1 cases are represented by solid and dashed lines, respectively.

described move toward the wall under outer normalization as the Reynolds number is increased [4]. After this point, the vertical-transport term $\overline{v'\omega_z'}$ is dominant with respect to $\overline{w'\omega_y'}$, as also documented by Klewicki [8] at higher Re, and the magnitude of $\overline{u'v'}$ decreases farther toward the centerplane. Finally, the spanwise-transport term becomes positive, $\overline{w'\omega_y'} > 0$, such that $\overline{w'\omega_y'} + \overline{v'\omega_z'} = 0$ and $\overline{u'v'} = \partial\overline{u'v'}/\partial y = 0$ at $y/h = 0$, where the horizontal symmetry plane is located. The vorticity-flux terms are reversed on the horizontal centerplane ($y/h = 0$), as shown in Fig. 1 (right). Note that on this plane $\overline{u'w'}$ is maximum and $\overline{u'v'} = 0$ due to symmetry. Similarly, when these profiles are scaled with the local friction velocity they show good agreement with the channel case in the near-wall region. On the other hand, the secondary flow has a strong impact on the profiles away from the wall. Note that additional simulations at higher Re will help to clarify the scaling behavior of the various fluxes when sufficient inner-outer separation is present in the flow.

The fact that the profiles of the vorticity-flux terms are reversed at the sidewalls implies that there must be a reversal point along the wall where $\overline{w'\omega_y'} \simeq 0$ and $\overline{v'\omega_z'} \simeq 0$. The two-dimensional contour plots of $\overline{v'\omega_z'}$ and $\overline{w'\omega_y'}$ are shown in Figs. 4.3 and 4.4 from Vidal [13], respectively, together with the corresponding mean and instantaneous transport terms. In the AR3r0 case the reversal abruptly occurs at the sharp corner, where $\overline{w'\omega_y'} \simeq \overline{v'\omega_z'} \simeq 0$ due to the overlap of the horizontal and vertical boundary layers. Note that in the near-corner region both vertical and spanwise fluctuations are inhibited by the walls. However, in case AR3r1 this effect is not present and the reversal occurs gradually throughout the beginning of the curved wall. Interestingly, the negative region of $\overline{w'\omega_y'}$ gradually evolves through the curved wall into the negative inner peak of the reversed profile at $y/h = 0$. Note that this peak is analogous to the positive inner peak of $\overline{v'\omega_z'}$ at $z/h = 0$. Similarly, the positive peak of $\overline{v'\omega_z'}$ at $z/h = 0$ gradually develops into the maximum value of $\overline{v'\omega_z'} > 0$ at $y/h = 0$, which is analogous to the minimum value of $\overline{w'\omega_y'}$ at $z/h = 0$.

In both cases, the mean transport terms $W\Omega_y$ and $V\Omega_z$ exhibit nonzero values in the reversal region. In the AR3r1 case, the mean transport terms compensate the gradual transition of the fluctuating terms leading to a more abrupt variation of the instantaneous terms $\overline{w\omega_y}$ and $\overline{v\omega_y}$. The phenomenon occurs in the transition point between the curved and straight walls, where $\overline{w\omega_y} \simeq \overline{v\omega_y} \simeq 0$. The secondary flow convects positive $\Omega_y$ along the horizontal symmetry plane ($y/h = 0$) toward the sidewalls ($W < 0$) and along the near-wall region toward the horizontal wall ($W > 0$). Similarly, negative $\Omega_z$ is driven toward the rounded walls ($V < 0$) and away ($V > 0$) from the straight walls. Therefore,

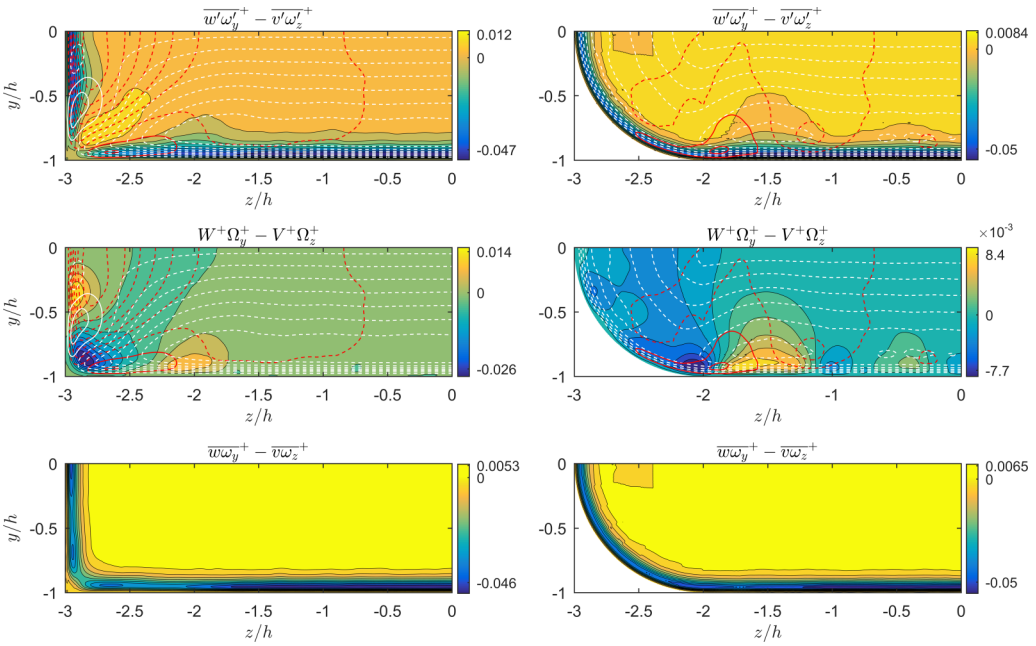


FIG. 2. Distributions showing ten contours of $(\overline{w'\omega'_y}^+ - \overline{v'\omega'_z}^+)$, $(W^+\Omega_y^+ - V^+\Omega_z^+)$, and $(\overline{w\omega_y}^+ - \overline{v\omega_z}^+)$. Top-left and middle-left panels: contours every 0.1 units of (white) $\overline{u'v'}^+$ and (black) $\overline{u'w'}^+$. Top-right and middle-right panels: contours every 0.1 units of (white) $\overline{u'_x u'_n}^+$ and (red) $\overline{u'_x u'_t}^+$, where $x$, $n$, and $t$ are the streamwise wall-normal and wall-tangent directions, respectively. Solid and dashed lines are used to denote positive and negative shear stresses. All quantities are scaled with $\nu$ and $u_{\tau,c}$.

the net effect of the secondary flow is to homogenize the mean wall-normal vorticity by reducing $\Omega_z$ on the straight wall and to increase $\Omega_y$ on the sidewalls. A similar behavior is observed in the AR3r0 case, where the secondary flow convects both $\Omega_z$ and $\Omega_y$ into the corner and away from the adjacent walls.

The distribution of $(\overline{w'\omega'_y} - \overline{v'\omega'_z})$ is shown in Fig. 2 (top) for the two cases under study together with the mean and instantaneous components. Interestingly, at some locations along the perimeter of the ducts the isolines of the distribution are lifted away from the wall, as can be clearly appreciated at $z/h \simeq -2$ and $y/h \simeq -0.5$ in the AR3r0 case and at $z/h \simeq -1.5$ in the AR3r1 case. The resulting distribution exhibits a negative region of $(\overline{w'\omega'_y} - \overline{v'\omega'_z})$ extending farther away from the wall. This behavior can be better understood by analyzing the distribution of the primary and secondary Reynolds shear stresses, which are also shown in Fig. 2. In the AR3r1 case, the primary Reynolds shear stress is rotated such that $u'_x$, $u'_n$, and $u'_t$ are the fluctuating streamwise, wall-normal and wall-tangent velocity components. These components are defined with respect to the closest wall and such that the rotated and the nonrotated components coincide on the horizontal wall. Note that the rotation does not affect the subtraction of both terms such that $\overline{w'\omega'_y} - \overline{v'\omega'_z} = \overline{u'_t\omega'_n} - \overline{u'_n\omega'_y}$. Consequently, $\overline{u'_x u'_n}$ and $\overline{u'_x u'_t}$ are the primary and secondary Reynolds shear stresses. The Reynolds shear stresses were not rotated in the AR3r0 case as there is no simple way to do this. Nevertheless, note that $\overline{u'v'}$ and $\overline{u'w'}$ are the primary and secondary Reynolds shear stresses on the horizontal wall, respectively, and their roles are reversed on the vertical wall.

The location where the isolines are lifted corresponds to the preferential location of an ejection ($u' < 0, v > 0$) [11], which generates the peak of $\overline{u'v'}$. Ejections are flanked by two counter-rotating streamwise vortices (see Kim [14]), which generate $\overline{u'w'} > 0$ on the left and $\overline{u'w'} < 0$ on the right of $z/h \simeq 1.5$. Therefore, both terms in Eq. (1) are negative ($\partial\overline{u'w'}/\partial z < 0$ and $\partial\overline{u'v'}/\partial y < 0$) and

stronger above the buffer layer, increasing the local value of $(\overline{w'\omega'_y} - \overline{v'\omega'_z})$. Furthermore, quadrant analysis and conditional averaging of these geometries reveal that the preferentially located ejections contribute to the mean cross-flow [11]. Note that in the AR3r0 case the maximum value of $(\overline{w'\omega'_y} - \overline{v'\omega'_z})$ is located near the sharp corner. In this region the isolines of the primary stresses concentrate leading to larger positive $\partial\overline{u'v'}/\partial y$ and $\partial\overline{u'w'}/\partial z$ values. The secondary shear stresses also contribute to the positive $\partial\overline{u'v'}/\partial y$ and $\partial\overline{u'w'}/\partial z$ values along the corner bisector.

The distribution of $(W^+\Omega_y^+ - V^+\Omega_z^+)$ is also shown in Fig. 2 (middle). Similarly, rotation does not affect the subtraction of both terms. This quantity is distributed such that $(\overline{w\omega_y} - \overline{v\omega_z})$ is homogeneous in the wall-tangent direction, as shown in Fig. 2 (bottom). Therefore, the transport of viscous stresses by the secondary flow opposes the increased turbulent shear-stress gradients. The behavior agrees with the main conclusion of Gessner [15], stating that the secondary flow is the direct result of the turbulent shear-stress gradients, and highlights the role of the secondary shear stresses. This relationship between the mean and fluctuating transport of vorticity is valuable to turbulence modeling of complex flows, and can contribute to the improvement of those turbulent models when it comes to accurately predicting the secondary flows [16], and to the development of novel data-driven modeling frameworks [17]. Note that simple eddy-viscosity models based on linear constitutive relations, such as the standard $\kappa - \epsilon$ model, fail to properly predict the mean cross-flow in turbulent ducts [18].

The mechanisms that contribute to the vorticity fluxes are further analyzed in the AR3r1 case. To this end, the homogeneity of the streamwise direction can be used to simplify the vorticity-flux terms $\overline{v'\omega'_z}$ and $\overline{w'\omega'_y}$ to $-\overline{v'\partial u'/\partial y}$ and $\overline{w'\partial u'/\partial z}$, respectively, as shown in Eq. (4). This simplification leads to the set of equations (5), which are also separately valid for the fluctuating, averaged and instantaneous quantities.

$$\overline{v'\omega'_z} = \overline{v'\frac{\partial v'}{\partial x}} - \overline{v'\frac{\partial u'}{\partial y}} = \frac{1}{2}\overbrace{\frac{\partial \overline{v'^2}}{\partial x}}^{0} - \overline{v'\frac{\partial u'}{\partial y}},$$

$$\overline{w'\omega'_y} = \overline{w'\frac{\partial u'}{\partial z}} - \overline{w'\frac{\partial w'}{\partial x}} = \overline{w'\frac{\partial u'}{\partial z}} - \frac{1}{2}\overbrace{\frac{\partial \overline{w'^2}}{\partial x}}^{0}. \tag{4}$$

$$\frac{\partial\overline{u'v'}}{\partial y} + \frac{\partial\overline{u'w'}}{\partial z} = \overline{v'\frac{\partial u'}{\partial y}} + \overline{w'\frac{\partial u'}{\partial z}},$$

$$\frac{\partial(UV)}{\partial y} + \frac{\partial(UW)}{\partial z} = V\frac{\partial U}{\partial y} + W\frac{\partial U}{\partial z}, \tag{5}$$

$$\frac{\partial\overline{uv}}{\partial y} + \frac{\partial\overline{uw}}{\partial z} = \overline{v\frac{\partial u}{\partial y}} + \overline{w\frac{\partial u}{\partial z}}.$$

The correlation between the instantaneous cross-flow and the in-plane derivatives of the fluctuating streamwise velocity is strongest in the buffer-layer region. This region is characterized by the presence of high- and low-velocity streaks which alternate in the spanwise direction and contribute to the nonzero $\partial u'/\partial z'$ and $\partial u'/\partial y'$ terms. Another important characteristic of the buffer layer is the presence of bursting events. The bursting events generate strong cross-flow fluctuations that contribute to the transfer of momentum between the near-wall region and the core of the flow. These events are often categorized with respect to the sign of the velocity fluctuations in the vertical $v'$ and streamwise $u'$ directions [19], as shown in Table II. In the present work, quadrant analysis and conditional averaging are used to analyze the contribution of the different types of bursting events to both fluxes. A similar approach was followed by Kim [14] to study the turbulence structures

TABLE II. Conditions used for quadrant analysis and conditional averaging.

| Event name | $u'$ | $v$ |
|---|---|---|
| Q1 or outward motion | + | + |
| Q2 or ejection | − | + |
| Q3 or inward motion | − | − |
| Q4 or sweep | + | − |

associated with the bursting events in turbulent channel flow. Doing so, the role of the near-wall streamwise vortices in the fluxes of vorticity is further characterized.

In plane channel and pipe flows, the behavior of bursting events is homogeneous in the wall-tangent direction, i.e., sweeps and ejections are homogeneously distributed in the spanwise (or azimuthal) direction and are as likely to turn in clockwise or anticlockwise directions. These events were analyzed in rectangular ducts with rounded sidewalls by Vidal *et al.* [11]. The authors showed that sweeps are preferentially located in the transition point between the curved sidewalls and the straight horizontal wall, where the mean cross-flow is maximum. Similarly, ejections tend to be located at the beginning of the horizontal wall and both types of events preferentially tilt toward the core of the flow. This behavior leads to an inhomogeneous distribution of the primary shear stresses in the wall-tangent direction. Similar observations were made in square and hexagonal ducts by Huser and Biringen [20] and Marin *et al.* [21]. Furthermore, Pinelli *et al.* [22] and Vinuesa *et al.* [23] showed in square and rectangular ducts that the near-wall quasistreamwise vortices are responsible for the nonzero mean streamwise vorticity $\Omega_x$. As discussed by Hallez and Magnaudet [24], in certain cases it is possible to predict some aspects of the secondary flow. For instance, in turbulent ducts of complex shape the secondary flow convects streamwise velocity away from the core toward the walls located farther away from it, and low-momentum fluid from the closer walls back to the core. Furthermore, sweeping events convect high-momentum fluid from the core of the duct to the near-wall region and ejections inject low-momentum fluid from the near-wall region into the core of the duct. Equations (5) show that a similar analogy is present between the instantaneous and mean vorticity fluxes. Therefore, the secondary flow could be associated with the inhomogeneous part of the vorticity fluxes.

The decomposition of $\overline{v'\omega_z'} = -\overline{v'\partial u'/\partial y}$ into the contributions from each type of event is shown in Fig. 3 for the AR3r1 case at $z/h = 0, -1.5$, and $-2$, respectively. Note that these are the locations

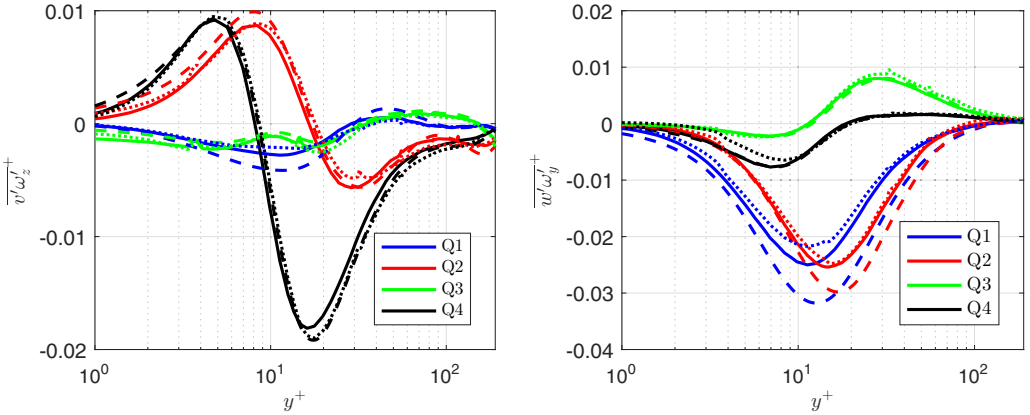


FIG. 3. Conditionally averaged $\overline{v'\omega_z'}^+$ and $\overline{v'\omega_z'}^+$ at $z/h = 0$ (solid line), $z/h = -1.5$ (dashed line), and $z/h = -2$ (dotted line), where the labels refer to the conditions in Table II. All quantities are scaled with $\nu$ and the local $u_\tau$.

of the vertical symmetry plane, the preferential position of ejections, and the transition between the curved and straight walls, respectively. The figure shows that the contribution to the vorticity-flux terms from each type of event are both qualitatively and quantitatively different.

First, we focus on a region very close to the wall where an ejection, i.e., a region of positive wall-normal $v > 0$ and negative streamwise fluctuating velocities $u' < 0$, is present. At the wall $u' = 0$, thus, $\partial u'/\partial y < 0$ and $-v'\partial u'/\partial y > 0$, a fact that explains the positive part of $\overline{v'\omega_z'}$ in the viscous sublayer. Since $v' > 0$ and both terms in $\overline{v'\omega_z'}$ are highly correlated in the near-wall region, $\overline{v'\omega_z'}$ is zero at $y^+ \simeq 11$ only if $\partial u'/\partial y = 0$. Therefore, the magnitude of $u' < 0$ associated with the ejections is maximum at $y^+ \simeq 11$, which is close to the location of the inner peak of the streamwise fluctuations $\overline{u'^2}$ at $y^+ \simeq 14$ (see, for instance, Jiménez and Moin [12]). After this point, the magnitude of $u' < 0$ decays in the wall-normal direction, thus, $\partial u'/\partial y > 0$ and $\overline{v'\omega_z'} < 0$.

Furthermore, the value $y^+ \simeq 11$ is also the location of the minimum value of the contribution from the ejections to $\overline{w'\omega_y'} = \overline{w'\partial u'/\partial z}$. In the near-wall bursting cycle, ejections are flanked by two counter-rotating streamwise vortices directed such that $w' > 0$ and $w' < 0$ on the left and right sides of the ejections, respectively. During an ejection event the magnitude of $u'$ is minimum with respect to the spanwise direction, i.e., $\partial u'/\partial z = 0$. Therefore, on the left side of the ejection $\partial u'/\partial z < 0$ and $w' > 0$, whereas on the right side $\partial u'/\partial z > 0$ and $w' < 0$ such that the term $w'\partial u'/\partial z$ is always negative and leads to $\overline{w'\omega_y'} < 0$. Note that the contribution from the ejections is much stronger in the $\overline{w'\omega_y'}$ profile at $z/h = -1.5$, where this type of event is preferentially located. The contribution to $\overline{v'\omega_z'}$ is also stronger at this location but to a lesser extent. The stronger negative $\overline{w'\omega_y'}$, which is caused by ejections and Q1 events, is responsible for the region of negative $(\overline{w'\omega_y'} - \overline{v'\omega_z'})$ away from the wall.

Second, we focus on a region very close to the wall exhibiting a sweeping event, i.e., negative wall-normal $v < 0$ and positive streamwise fluctuating velocities $u' > 0$. The contribution of the sweeping events to the $\overline{v'\omega_z'}$ distribution is qualitatively similar to that of the ejections, although weaker in the viscous sublayer, and can be explained with equivalent arguments. At the wall $u' = 0$, thus, $\partial u'/\partial y > 0$ and $-v'\partial u'/\partial y > 0$, which again leads to a positive contribution to $\overline{v'\omega_z'}$ below the buffer layer. In this case, $\overline{v'\partial u'/\partial y} = 0$ at $y^+ \simeq 8$, and $\partial u'/\partial y < 0$ after this point. This behavior indicates that sweeping events turn in the wall-tangent direction at $y^+ \simeq 8$ generating a spanwise layer of maximum $u' > 0$. Note that the maximum value of $u'$ in a sweeping event is located closer to the wall than the minimum value of $u'$ corresponding to an ejection, since sweeping events are directed toward the wall and ejections away from it. Therefore, the opposite wall-normal directions associated with both types of events explains the phase difference of their contributions to $\overline{v'\omega_z'}$. Finally, note that the contribution from the sweeping events to the $\overline{v'\omega_z'}$ profile is slightly stronger at $z/h = -1.5$ and $-2$, where these events are preferentially located.

Interestingly, the point where $\partial u'/\partial y = 0$ also corresponds to the maximum contribution from the sweeps to $\overline{w'\omega_y'} = \overline{w'\partial u'/\partial z} < 0$. As sweeping events turn in the wall-tangent direction they generate wall-tangent velocity fluctuations that convect the high-momentum fluid in this direction. Note that the positive spanwise fluctuations $w' > 0$ generate $\partial u'/\partial z < 0$, whereas the negative ones $w' < 0$ generate $\partial u'/\partial z < 0$. However, the contribution of sweeping events to $\overline{w'\omega_y'}$ is significantly lower.

Finally, the contribution of outward motions or Q1 events to $\overline{w'\omega_y'}$ is very similar to the one corresponding to the ejections. Both distributions have similar minimum values and are shifted in the wall-normal direction by roughly one viscous unit. However, Q1 events are much more unlikely to occur in the near-wall region than ejections, which means that the contribution from this type of events is stronger and short-lived. This strong intermittent behavior was already reported by Brown *et al.* [5]. These authors calculated the probability density function (pdf) of $\overline{w'\omega_y'}^+$ at $y^+ = 5$, as shown in Fig. 2 from Brown *et al.* [5]. Note that the contribution of the Q1 events at $y^+ = 5$ is stronger than the sum of all the other contributions and explains the high kurtosis present in their pdf. Interestingly, inward motions or Q3 events also play a relevant role generating $\overline{w'\omega_y'} > 0$ at $y^+ > 10$ and are

mainly responsible for the $\overline{w'\omega'_y} > 0$ present at $y^+ > 40$. Note that Q1 events are also preferentially located at $z/h = -1.5$, which increases their local contribution to the $\overline{w'\omega'_y}$ profile. Moreover, their contribution is weaker at $z/h = -2$, where sweeping events are preferentially located.

To summarize, the vorticity-flux terms ($\overline{w'\omega'_y}^+$ and $\overline{v'\omega'_z}^+$) are analyzed in fully developed rectangular ducts with straight and semicylindrical sidewalls with $AR = 3$. The mean vorticity transport terms ($W^+\Omega_y^+$ and $V^+\Omega_z^+$), caused by the secondary motions of Prandtl's second kind, and the corresponding time average of the instantaneous products ($\overline{w\omega_y}^+$ and $\overline{v\omega_z}^+$) are also analyzed showing that the same equations apply to all of these terms in fully developed flow. The results on the vertical symmetry plane ($z/h = 0$) share some similarities with those corresponding to the channel case by Brown *et al.* [5]. On the horizontal symmetry plane ($y/h = 0$), the profiles are reversed and with opposite signs but are similar to the channel case in the near-wall region when scaled with the local friction velocity. The transition from the former to the latter configurations occurs abruptly on the sharp corner and gradually throughout the curved wall.

The secondary flow is responsible for the mean vorticity-flux terms located in the transition region. The net effect of the secondary flow is to homogenize the mean wall-normal vorticity by reducing $\Omega_z$ on the straight wall and increasing $\Omega_y$ on the sidewalls. Furthermore, the transport of viscous stresses by the secondary flow locally counteracts the inhomogeneous wall-tangent distribution of in-plane turbulent shear-stress gradient, which is located around $z/h = -1.5$. Therefore, a relationship between the mean and fluctuating transport terms was established showing that the vorticity-flux approach can provide useful insights to the turbulence modeling of secondary motions and three-dimensional flows.

The role of the bursting events is evaluated using quadrant analysis to compute the conditionally averaged contribution to $\overline{w'\omega'_y}^+$ and $\overline{v'\omega'_z}^+$ from each type of bursting event. Ejections and sweeps are the main contributors to $\overline{v'\omega'_z}^+$ and their profiles are shifted in the wall-normal direction by roughly three viscous units. Both types of events generate $\overline{v'\omega'_z}^+ > 0$ below the buffer layer and $\overline{v'\omega'_z}^+ < 0$ above it. The transition point given by $\overline{v'\omega'_z}^+ = 0$ occurs at the vertical location where the magnitude of the streamwise fluctuations associated with the event is maximum, which is close to the near-wall peak of the $\overline{u'^2}$ profile. Sweeping events are also an important contribution to the spanwise-transport term generating $\overline{w'\omega'_y}^+ > 0$ in the logarithmic region. However, ejections and Q1 events are the main contributors to these terms producing $\overline{w'\omega'_y}^+ < 0$ everywhere. This analysis also reveals that the inhomogeneous region of in-plane turbulent shear stress around $z/h = -1.5$ is mainly caused by preferentially located ejections and Q1 events leading to a stronger $\overline{w'\omega'_y}^+$ term.

We thank Professor Brown for pointing out this approach to us and motivating the present study. Computer time was provided by the Argonne Leadership Computing Facility at Argonne National Laboratory, which is supported by the Office of Science of the U.S. Department of Energy. R.V. acknowledges the financial support from the Swedish Research Council (VR).

[1] G. I. Taylor, Eddy motion in the atmosphere, Philos. Trans. R. Soc. A **215**, 1 (1915).

[2] L. W. B. Browne, R. A. Antonia, and D. A. Shah, Characteristics of vorticity fluctuations in a turbulent wake, J. Fluid Mech. **189**, 349 (1988).

[3] K. T. Christensen and R. J. Adrian, The velocity and acceleration signatures of small-scale vortices in turbulent channel flow, J. Turbul. **3**, 23 (2002).

[4] G. L. Eyink, Turbulent flow in pipes and channels as cross-stream "inverse cascades" of vorticity, Phys. Fluids **20**, 125101 (2008).

[5] G. Brown, M. Lee, and R. Moser, Vorticity transport: the transfer of viscous stress to Reynolds stress in turbulent channel flow, in *Proceedings of the 9th International Symposium on Turbulence and Shear Flow Phenomena (TSFP-9)*, Melbourne, Australia, 2015.

[6] G. Brown, Re-laminarization and re-transition of a turbulent boundary layer from a vorticity point of view, in *Proceedings of the 10th International Symposium on Turbulence and Shear Flow Phenomena (TSFP-10)*, Chicago, 2017.
[7] L. Prandtl, *Essentials of Fluid Dynamics* (Blackie, Glasgow, 1952), p. 145.
[8] J. C. Klewicki, Velocity-vorticity correlations related to the gradients of the Reynolds stresses in parallel turbulent wall flows, Phys. Fluids A **1**, 1285 (1989).
[9] P. F. Fischer, J. Lottes, and S. Kerkemeier, Nek5000 Web page, http://nek5000.mcs.anl.gov.
[10] R. Vinuesa, P. Schlatter, and H. M. Nagib, Secondary flow in turbulent ducts with increasing aspect ratio, Phys. Rev. Fluids **3**, 054606 (2018).
[11] A. Vidal, R. Vinuesa, P. Schlatter, and H. M. Nagib, Turbulent rectangular ducts with minimum secondary flow, Int. J. Heat Fluid Flow **72**, 317 (2018).
[12] J. Jiménez and P. Moin, The minimal flow unit in near-wall turbulence, J. Fluid Mech. **225**, 213 (1991).
[13] A. Vidal, Direct numerical simulations of turbulent wall-bounded flows in moderately complex geometries, Ph.D. thesis, Illinois Institute of Technology, 2017.
[14] J. Kim, Turbulence structures associated with the bursting event, Phys. Fluids **28**, 52 (1985).
[15] F. B. Gessner, The origin of secondary flow in turbulent flow along a corner, J. Fluid Mech. **58**, 1 (1973).
[16] P. R. Spalart, A. Garbaruk, and A. Stabnikov, On the skin friction due to turbulence in ducts of various shapes, J. Fluid Mech. **838**, 369 (2018).
[17] J. Weatheritt and R. Sandberg, A novel evolutionary algorithm to algebraic modifications of the RANS stress-strain relationship, J. Comput. Phys. **325**, 22 (2016).
[18] P. R. Spalart, Strategies for turbulence modelling and simulations, Int. J. Heat Fluid Flow **21**, 252 (2000).
[19] S. S. Lu and W. W. Willmarth, Measurements of the structure of the Reynolds stress in a turbulent boundary layer, J. Fluid Mech. **60**, 481 (1973).
[20] A. Huser and S. Biringen, Direct numerical simulation of turbulent flow in a square duct, J. Fluid Mech. **257**, 65 (1993).
[21] O. Marin, R. Vinuesa, A. V. Obabko, and P. Schlatter, Characterization of the secondary flow in hexagonal ducts, Phys. Fluids **28**, 125101 (2016).
[22] A. Pinelli, M. Uhlmann, A. Sekimoto, and G. Kawahara, Reynolds number dependence of mean flow structure in square duct turbulence, J. Fluid Mech. **644**, 107 (2010).
[23] R. Vinuesa, C. Prus, P. Schlatter, and H. M. Nagib, Convergence of numerical simulations of turbulent wall-bounded flows and mean cross-flow structure of rectangular ducts, Meccanica **51**, 3025 (2016).
[24] Y. Hallez and J. Magnaudet, Turbulence-induced secondary motion in a buoyancy-driven flow in a circular pipe, Phys. Fluids **21**, 081704 (2009).